J Appl Electrochem (2014) 44:647–654
DOI 10.1007/s10800-014-0671-5

RESEARCH ARTICLE

Electrical and electrochemical properties of molten-salt-synthesized 0.05 mol Zr- and Si-doped $Li_4Ti_5O_{12}$ microcrystals

V. D. Nithya · S. Sharmila · Kumaran Vediappan · Chang Woo Lee · Leonid Vasylechko · R. Kalai Selvan

Received: 7 October 2013 / Accepted: 27 January 2014 / Published online: 12 February 2014

Abstract This work emphasizes the structural, morphological, electrical, and electrochemical properties of 0.05 mol Zr- and Si-doped $Li_4Ti_5O_{12}$ synthesized using the molten salt method and applied to negative electrodes in Li-ion batteries. Formation of the spinel phase with face-centered cubic structure in the nominally pure and Zr- and Si-doped samples are revealed from X-ray powder diffraction technique. Lattice parameters refined by full-profile Rietveld method are in accordance with the literature data for the $Li_4Ti_5O_{12}$ ($Li_{1.333}Ti_{1.667}O_4$) spinel structure. The presence of possible functional groups is identified using Fourier transform infra red spectroscopy. The field emission scanning electron microscopic images indicate the formation of micron-sized (1.5–2 μm) randomly distributed polyhedral-shaped particles. The electrical conductivity studies demonstrate the grain-conducting behavior of the material. The maximum DC conductivity of 2×10^{-5} S cm^{-1} is observed for Zr-doped $Li_4Ti_5O_{12}$ at room temperature. The galvanostatic charge–discharge studies show that Zr-doped $Li_4Ti_5O_{12}$ exhibits a high discharge capacity of about 325 mAh g^{-1} at 0.01 °C, higher than Si-doped $Li_4Ti_5O_{12}$ (200 mAh g^{-1}), and also that the cycling stability of Zr-doped $Li_4Ti_5O_{12}$ is enhanced.

Keywords $Li_4Ti_5O_{12}$ · X-ray diffraction · Electrical conductivity · Cole–cole plot · Charge–discharge studies

V. D. Nithya · S. Sharmila · R. Kalai Selvan (✉)
Solid State Ionics and Energy Devices Laboratory, Department of Physics, Bharathiar University, Coimbatore 641 046, India
e-mail: selvankram@buc.edu.in

K. Vediappan · C. W. Lee (✉)
Department of Chemical Engineering, College of Engineering, Kyung Hee University, 1732 Deogyeong-daero, Gihung, Yongin 446-701, South Korea
e-mail: cwlee@khu.ac.kr

L. Vasylechko
Semiconductor Electronics Department, Lviv Polytechnic National University, 12 Bandera Street, Lviv 79013, Ukraine

1 Introduction

Lithium-ion batteries have attracted much interest in the scientific community due to their high energy density, light weight, easy handling, high cell voltage, safe operations, long cycle life, and low self-discharge. Because of these desirable properties, they are widely used in diverse applications such as cell phones, PCs, camcorders, electric vehicles, and aerospace. The commonly used graphite anode in Li-ion batteries exhibits an excellent cycling behavior, but the main drawback is the moderate theoretical capacity of 372 mAh g^{-1} (LiC_6). The other problem observed is electrolyte reduction during Li intercalation into graphitic layers, which causes the formation of a solid-electrolyte interface layer (SEI), which also decreases the life span of a battery [1]. Therefore, researchers must identify a suitable material for the anodes that possesses higher capacity and a better life span than carbon. One category of promising materials for metallic anodes includes Si ($Li_{4.4}Si$; 4,200 mAh g^{-1}), Sn ($Li_{4.4}Sn$; 993 mAh g^{-1}), and Ge ($Li_{3.75}Ge$; 1,385 mAh g^{-1}). Their major drawback is that volume changes occur in the electrodes during Li alloying/de-alloying that leads to capacity fading during extended cycles [2–4]. Another category is transition metal oxides such as NiO, AMn_2O_4 (Co, Ni, Zn), TiO_2, and SnO_2 [5–7], which possess better rate capability and are low cost and environmentally friendly. Among the transition metal oxides, spinel-structured $Li_4Ti_5O_{12}$ is an

attractive anode material for Li-ion batteries since it has a zero-strain effect that results in negligible changes in the unit cell volume during lithium-ion intercalation and deintercalation, a high charge/discharge plateau, a capacity of up to 175 mAh g^{-1}, prevention of SEI layer formation, and a potential voltage of 1.5 V versus those of Li metal [8].

There are many reports on the use of $Li_4Ti_5O_{12}$ as an anode material in Li-ion batteries synthesized using various techniques, such as molten salt [9], solution precipitation [10], solid–state reaction [11], sol–gel [12], cellulose-assisted combustion [13], solvothermal [14], hydrothermal [15], microwave [16], and pulsed laser deposition [17]. The main drawback of $Li_4Ti_5O_{12}$ is that it possesses reduced electronic conductivity. Hence, to improve the electrical conductivity, research has focused on doping with an aliovalent metal ion [18–24] or coating with conductive carbon [25, 26]. Doping in Ti^{4+} or O^{2-} sites increases the mixing of Ti^{3+}/Ti^{4+} for charge composition and improves the electrical conductivity. There are also reports on $Li_4Ti_5O_{12}$-doped with various metal ions, including spinel $Li_4Ti_{5-x}V_xO_{12}$ $(0 \leq x \leq 0.3)$ [18] and $Li_{4-x}Al_xTi_5O_{12}$ $(x = 0.0, 0.05, 0.1, 0.2)$ [19], Br-doped $Li_4Ti_5O_{12}$ [20], $Li_{4-x}Mg_xTi_{5-x}V_xO_{12}$ $(0 \leq x \leq 1)$ [21], Ag-doped $Li_4Ti_5O_{12}$ using a solid–state reaction [22], Cr^{3+}-, Mn^{3+}-, Ni^{3+}-, and Co^{3+}-doped $Li_4Ti_5O_{12}$ [23], and Nb-doped $Li_4Ti_5O_{12}$ using the sol–gel method [24].

In the present work we exploit Si^{4+} and Zr^{4+} ions as the dopant for Ti^{4+} in $Li_4Ti_5O_{12}$. The molten salt method was selected as the synthesis technique since it is the simplest, most cost effective, and versatile method for the preparation of a pure and single-phase powder. Furthermore, this is a single-step process with no need for any complicated instrumentation or organic additives and which also prevents agglomeration. Subsequently, the prepared samples were characterized using X-ray diffraction (XRD), Rietveld refinement, Fourier transform infra red spectroscopy (FT-IR), field emission scanning electron microscope (FESEM), transmission electron microscope (TEM), AC impedance, and electrochemical charge–discharge analysis. In the present work, the material has been discharged to 0 V because replacing graphite with this zero-strain material could cause a decrease in cell voltage, thereby affecting its energy density. Many researchers thought that lithium could not be inserted into lithium titanate material at lower voltages. This concept was proved to be wrong by Ge et al. [27]. They illustrated that the theoretical capacity for $Li_4Ti_5O_{12}$ discharged to 0 V would be higher than for that discharged to 1 V because of the increase in the number of Li-ions intercalated/de-intercalated upon discharge to 0 V. Many studies based on the electrochemical performance of $Li_4Ti_5O_{12}$ anodes discharged to 0 V have been reported, as in the case of Mo-doped $Li_4Ti_5O_{12}$ [28], Ru-doped $Li_4Ti_5O_{12}$ [29], La-modified $Li_4Ti_5O_{12}$ [30], and Mn-doped $Li_4Ti_5O_{12}$ [31].

2 Experimental procedures

The typical synthesis of spinel $Li_4Ti_5O_{12}$ anode materials via the molten salt method is given elsewhere [31]. We performed a similar procedure for Zr- and Si (0.05 mol)-doped $Li_4Ti_5O_{12}$ using precursors of $Na_2SiO_3{\cdot}9H_2O$ and $ZrOCl_2$ in the stoichiometric ratio. The phase and structural characterization was conducted with XRD using a BRUKER diffractometer with Cu Kα radiation, a FT-IR using Shimadzu/Nicolet instruments in the range from 400–4,000 cm^{-1}, FESEM using Leo Supra 55, Genesis 2,000, and Carl Zeiss, and charge–discharge studies using a cycler (BT2000, Arbin). The 2100F JEOL instrument is used to envisage the TEM images. The electrical studies are done by using a computer-controlled HIOKI 3532 LCR HITESTER in the frequency range from 50 Hz to 10 kHz. For impedance measurements, the power was made into pellets 1 cm in diameter, and then silver paste was applied on both the flat surfaces. The pellet was placed between the two metallic electrodes of the sample holder for further measurements. The detailed electrode preparation and the electrochemical charge–discharge analysis were given elsewhere [31].

3 Results and discussion

3.1 Phase composition and structural properties

The XRD patterns of the nominally pure $Li_4Ti_5O_{12}$ [31] and Zr- and Si-doped samples are shown in Fig. 1(a–c). The diffraction peaks of all samples are sharp and well-defined, indicating the highly crystalline nature of the materials. The diffraction peaks of nominally pure and Zr-doped samples indicate a face-centered cubic spinel structure with an *Fd3m* space group and the pattern matches well with the JCPDS data No. 26-1198 and JCPDS 49-207, thus proving the formation of $Li_4Ti_5O_{12}$ phase [32]. Close examination of XRD patterns of these samples shows that besides of the main spinel phase, they contain a small amount of Li_2TiO_3 (JCPDS 33-831). According to the full-profile Rietveld refinement, performed by means of WinCSD programme package [33], the amount of minority Li_2TiO_3 phase in the nominally pure and Zr-doped samples is 8 and 13 wt%, respectively. In the refinement procedure the lattice parameters of both phases were refined together with background and peak profile parameters and correction of absorption and instrumental sample shift. Positional and displacement atomic parameters were refined for the

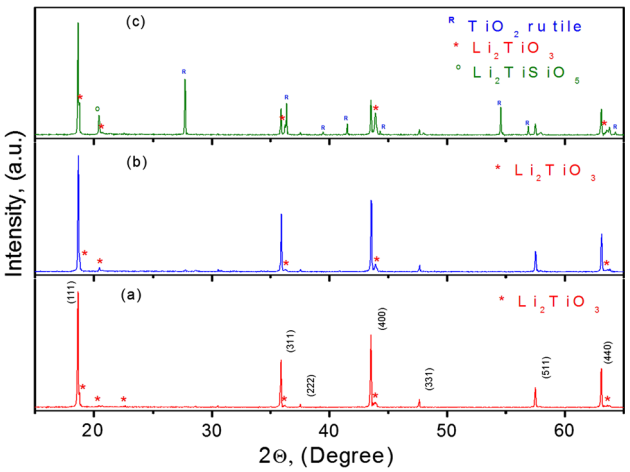

Fig. 1 XRD patterns of $Li_4Ti_5O_{12}$ (**a**) Zr- (**b**), and Si (**c**)-doped $Li_4Ti_5O_{12}$

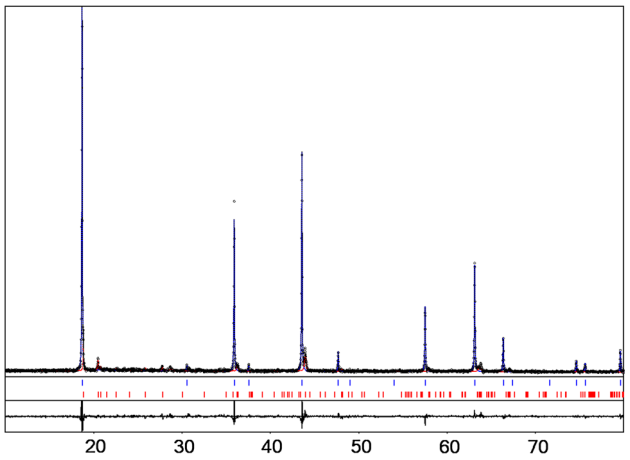

Fig. 2 Graphical results of multiphase Rietveld refinement showing coexistence of $Li_4Ti_5O_{12}$ (*blue*) and Li_2TiO_3 (*red*) phases in the Zr-doped $Li_4Ti_5O_{12}$. Experimental XRD pattern is shown in comparison with the calculated patterns. The difference between measured and calculated profiles is shown as a *curve* below the diagrams. *Short vertical bars* indicate the positions of diffraction maxima of $Li_4Ti_5O_{12}$ and Li_2TiO_3 (*upper* and *lower rows*, respectively). (Color figure online)

main $Li_4Ti_5O_{12}$ phase. As starting models for this refinement, the atomic positions as in $Li_{1.333}Ti_{1.667}O_4$ [34] and Li_2TiO_3 [35] were used. The graphical results of Rietveld refinement of the Zr-doped sample are presented in Fig. 2. The refined lattice parameters (Table 1) for nominally pure and Zr-doped $Li_4Ti_5O_{12}$—8.3571(4) and 8.3579(1) Å, respectively are practically the same within the limits of errors, and correspond to the literature data for the parent compound. Because of the ionic radius of Zr^{4+} species is practically equal to the radii of Li^+ and Ti^{4+} ions, the partial substitution of Zr for the Li or Ti sites do not affect

Table 1 Refined values of the lattice parameters and cell volumes of the spinel phases in the undoped, 0.05 mol Zr- and Si-doped samples

Compounds	a (Å)	V (Å^3)
$Li_4Ti_5O_{12}$	8.3571(4)	583.66(8)
Zr-doped $Li_4Ti_5O_{12}$	8.3579(1)	583.84(3)
Si-doped $Li_4Ti_5O_{12}$	8.3580(9)	583.9(2)
JCPDS 49-207	8.3588	

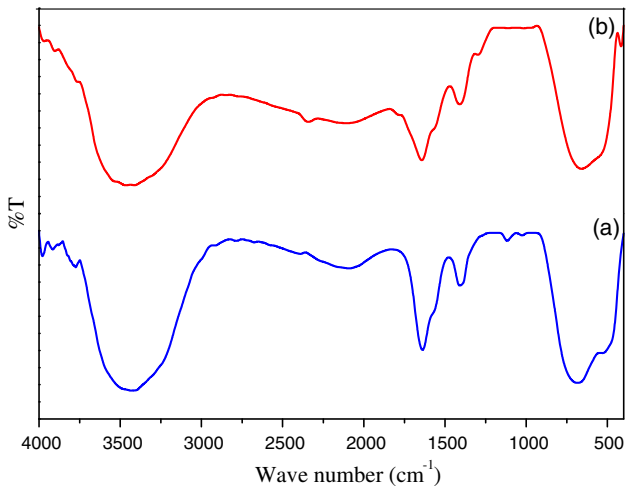

Fig. 3 FTIR spectra of 0.05 mol doped Zr- (*a*) and Si (*b*)-doped $Li_4Ti_5O_{12}$

the cell dimensions of the $Li_4Ti_5O_{12}$ structure. However, from the careful refinement of the displacement parameters and site occupancies of atoms in the Zr-doped $Li_4Ti_5O_{12}$ structure it can be concluded that Zr species partially occupy both tetrahedral (Li) and octahedral (Ti) sites.

Different phase behavior was observed in the Si-doped sample. Besides the $Li_4Ti_5O_{12}$ phase, the sample contains considerable amount of the TiO_2 rutile and Li_2TiO_3-related phase in the tentative weight proportion of 40:35:25 (Fig. 1c). In addition, one extra diffraction peak at 20.17° (2θ) point on the presence of one more phase, which could be identified as Li_2TiSiO_5 (JCPDS 13-268).

The FT-IR spectra of Zr- and Si-doped $Li_4Ti_5O_{12}$ are shown in Fig. 3. It is mainly used to identify the stretching and bending vibrations of the tetrahedral and octahedral complexes. Several bands were observed that were assigned to the broad stretching band of OH^- (3,409 cm^{-1}) and the strong asymmetric stretching band of COO^- (1,643.68 cm^{-1}). In case of pristine $Li_4Ti_5O_{12}$, strong low frequency bands observed at 697.25 cm^{-1} correspond to symmetric stretching vibrations of the octahedral MO_6 lattice [31, 36]. The symmetric stretching peaks of Si-doped $Li_4Ti_5O_{12}$ were shifted from 697.25 to 660.87 cm^{-1}

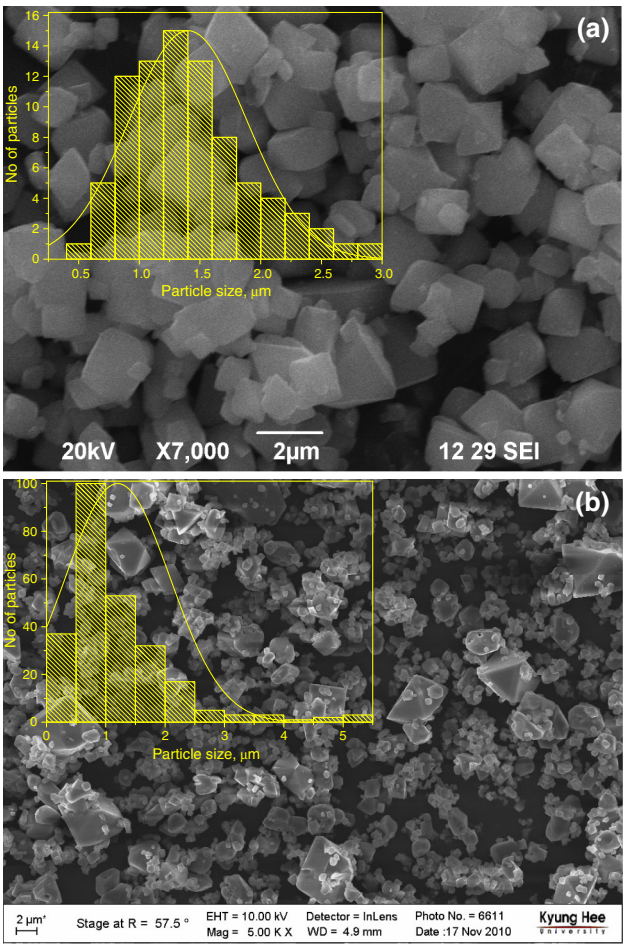

Fig. 4 FESEM images of 0.05 mol Zr- (**a**) and Si (**b**)-doped $Li_4Ti_5O_{12}$ (*inset* corresponding histogram)

and from 697.25 to 685.49 cm^{-1} for Zr-doped $Li_4Ti_5O_{12}$. The addition of dopant causes a shift in the Ti–O stretching band, implying that the dopants enter into the lattice site of the $Li_4Ti_5O_{12}$ material. The additional band at 415.89 cm^{-1} observed in the case of Si-doped $Li_4Ti_5O_{12}$ corresponds to the asymmetric stretching vibration of Si–O–Si bending vibrations [37]. In spite no crystalline SiO_2 phases were observed in the diffraction pattern, presence of silica in amorphous (cryptocrystalline) form could not be ruled out. The weak absorption peak located around 2,000 cm^{-1} is attributed to the adsorbed CO_2 on the surface of the material for $Li_4Ti_5O_{12}$.

3.2 Morphological analysis

The morphology of Zr- and Si-doped $Li_4Ti_5O_{12}$ is analyzed using FESEM, as shown in Fig. 4. The corresponding particle size histogram is given as inset of Fig. 4. The FESEM image of Zr-doped $Li_4Ti_5O_{12}$ (Fig. 4a) shows uniform morphology distributed evenly without any agglomeration. The advantage of the molten salt synthesis is that the reaction takes place in a liquid medium at high temperatures, which results in uniformly shaped particles without agglomerations. In the case of $Li_4Ti_5O_{12}$ reported earlier, the particles were found to be polyhedral in shape, and their size was in the vicinity of 1.75 μm [31]. The particle size histogram of Zr-doped $Li_4Ti_5O_{12}$ (Figure. 4(a) inset) shows that the maximum number of particles are in the vicinity of 1.2–1.3 μm without any agglomerations, and the sizes are found to be reduced compared with the parent $Li_4Ti_5O_{12}$. Similarly, the FESEM images of Si-doped $Li_4Ti_5O_{12}$ show that the particles were randomly distributed with irregular shapes and were distorted due to the presence of coarse particles. The particle sizes decreased to 0.5–1 μm with the addition of dopant. From the morphological point of view, the particle size reduction would favor capacity enhancement of the material. It is to be noted that, in the case of Zr-doped $Li_4Ti_5O_{12}$, no coarse particles were observed, which confirms that the Zr dopants are entered well into the lattice as evidenced in the XRD results. The well entered Zr ions into the lattice size effectively reduces the particle size, thereby enhancing the overall performance of the material. Overall, the highly crystalline nature of $Li_4Ti_5O_{12}$, both with and without dopant material, suggests that it would enhance the charge–discharge cycling stability to a great extent.

3.3 Electrical conductivity analysis

The electrical conductivities of $Li_4Ti_5O_{12}$, Zr- and Si-doped $Li_4Ti_5O_{12}$ were analyzed using AC impedance spectroscopy, which were employed to analyze the contributions of various electro-active regions (grain or grain boundaries or interfacial polarization) that have dominant effects in the electrical conductivity mechanism of the material. Figure 5 shows the measured room temperature Cole–Cole plot of $Li_4Ti_5O_{12}$, Zr- and Si-doped $Li_4Ti_5O_{12}$. It shows that the formation of a single semicircle, which indicates that the conductivity is mainly due to the bulk effect, i.e., grain conduction. The absence of a second semicircle implies that there is no grain boundary conduction occurring in the material. The single semicircle observed in all the cases corresponds to the parallel combination of bulk capacitance C_b and bulk resistance R_b. The bulk resistance of the material is measured based on the intercept of the radius of the semicircle with the x-axis. The calculated bulk resistance of Zr-doped $Li_4Ti_5O_{12}$ (9.017×10^6 Ω) is lower than the pristine $Li_4Ti_5O_{12}$ (1.6526×10^5 Ω). So the Zr-doped $Li_4Ti_5O_{12}$ possesses high conductivity compared with the parent $Li_4Ti_5O_{12}$. In contrast, in the case of Si-doped $Li_4Ti_5O_{12}$ (2.8954×10^5 Ω), the bulk resistance is increased compared with the parent; i.e., the conductivity is decreased for Si-doped $Li_4Ti_5O_{12}$, which might be due to the formation of Li_2TiSiO_5 impurities that impede electronic conduction. A similar

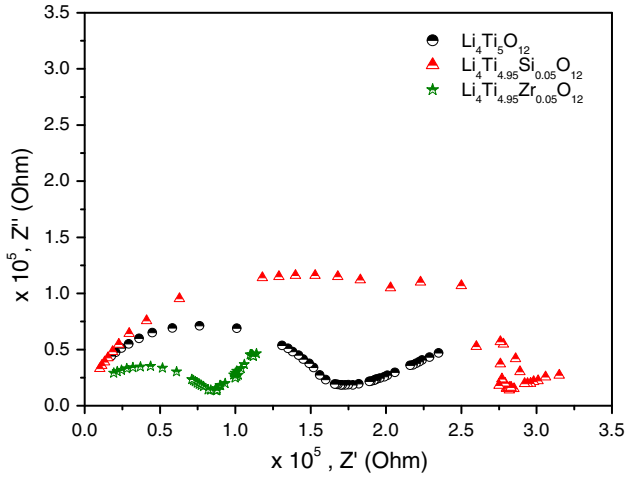

Fig. 5 Cole–Cole plot of doped and undoped $Li_4Ti_5O_{12}$

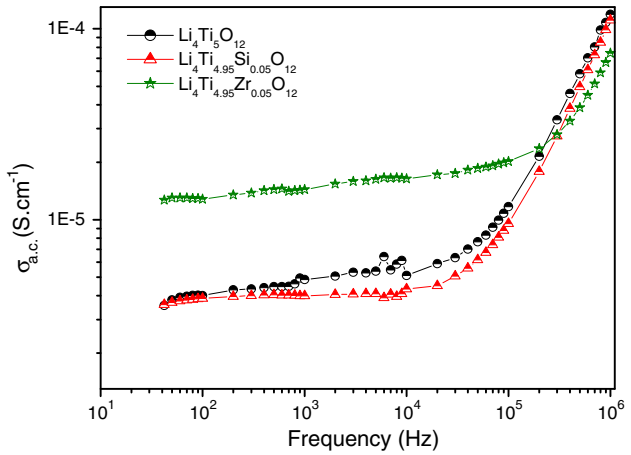

Fig. 6 Conductance spectra of doped and undoped $Li_4Ti_5O_{12}$

result was observed in the case of $CuFe_2O_4/SnO_2$ by Kalai Selvan et al. [38].

Figure 6 shows the conductance spectra of $Li_4Ti_5O_{12}$, Zr- and Si-doped $Li_4Ti_5O_{12}$ measured at room temperature. A frequency-independent region at lower frequencies and a frequency dispersion region at higher frequencies are observed for all the materials. The conductance spectra are found to obey Jonscher's power law [39]. The frequency-independent region at lower frequencies corresponds to the DC conductivity, and the observed behavior is inconsistent with the impedance analysis. Among these, Zr-doped $Li_4Ti_5O_{12}$ possesses high conductivity (2×10^{-5} S cm^{-1}) compared with the parent $Li_4Ti_5O_{12}$ (4.34×10^{-6} S cm^{-1}) at room temperature. A similar result was reported by Li et al. [40] for $Li_4Ti_{4.95}Zr_{0.05}O_{12}$; they stated that the electronic conductivity increases when Zr ions are completely substituted into the Ti site of $Li_4Ti_5O_{12}$. It is also to be noted from the figure that the conductivity value is decreased for Si-doped $Li_4Ti_5O_{12}$ (3.75×10^{-6} S cm^{-1}) compared with both $Li_4Ti_5O_{12}$ and Zr-doped $Li_4Ti_5O_{12}$. This decrease is due to enhancement in the barrier property upon the formation of secondary-impurity Li_2TiSiO_5. This may also be due to the addition of smaller ionic radii atoms Si^{4+} (0.026 nm) into Ti^{4+} (0.056 nm), which would cause lattice distortions due to the suppression of lattice conduction paths [41].

3.4 Electrochemical studies

The charge–discharge behavior of Zr- and Si-doped $Li_4Ti_5O_{12}$ studied in 2,032 coin cells versus those of lithium metal are shown in Fig. 6. The cell was charged to 3.0 V versus Li/Li^+ and discharged to 0 V versus Li/Li^+ under a constant current density of 0.1 mA cm^{-2}. Knowledge of the structure and electrochemical reaction of $Li_4Ti_5O_{12}$ during Li-ion intercalation/de-intercalation is needed for the study of charging–discharging profiles. The $Li_4Ti_5O_{12}$ structure has 75 % of the Li^+ ions located at tetrahedral 8a sites, while the remaining 25 % of the Li^+ and Ti^{4+} are randomly distributed in the octahedral 16d sites, with O^{2-} occupying the 32e sites, and the 8b, 48f, and 16c sites empty [42]. The electrochemical reaction involved is

$$[\mathrm{Li}]_{8a}\left[\mathrm{Li}_{1/3}\mathrm{Ti}_{5/3}\right]_{16d}[\mathrm{O}_4]_{32e} \rightleftarrows [\mathrm{Li}_2]_{16c}\left[\mathrm{Li}_{1/3}\mathrm{Ti}_{5/3}\right]_{16d}[\mathrm{O}_4]_{32e}.$$

During Li intercalation, Li at the 8a sites shifts to the 16c sites, and the number of free octahedral sites determines the overall capacity of $Li_4Ti_5O_{12}$. Normally, the theoretical capacity of $Li_4Ti_5O_{12}$ is 175 mAh g^{-1} due to the possibility of intercalation of 3 Li ions into $Li_4Ti_5O_{12}$ to form $Li_7Ti_5O_{12}$ when it is discharged to 1 V. In the case when it is discharged to 0 V, the theoretical capacity is 293 mAh g^{-1}. The reason behind this is described by Ge et al. through the core–shell model [27]: a two-phase conversion occurs in which $Li_4Ti_5O_{12}$ is first transformed to $Li_7Ti_5O_{12}$ and then further to $Li_{8.5}Ti_5O_{12}$ when discharged to 0 V. The insertion/de-insertion mechanism of lithium ions into/from $Li_7Ti_5O_{12}$ is given as

$$\mathrm{Li}_{6(16c)}\left[\mathrm{LiTi}_3^{3+}\mathrm{Ti}_2^{4+}\right]_{(16d)}\mathrm{O}_{12(32e)} + 2\mathrm{e}^- + 2\mathrm{Li}^+ \rightleftarrows \mathrm{Li}_{2(8a)}\mathrm{Li}_{6(16c)}\left[\mathrm{LiTi}_5^{3+}\right]_{(16d)}\mathrm{O}_{12(32e)}.$$

The same research group also found that the spinel $Li_4Ti_5O_{12}$ could accommodate 5 Li ions in the potential from 2.5 to 0.01 V, corresponding to the theoretical capacity of 293 mAh g^{-1}. A detailed sketch illustrating this behavior was given by Tian et al. [43]. As Fig. 6 shows, the initial discharge capacity of pristine $Li_4Ti_5O_{12}$ is 234.69 mAh g^{-1}, and the discharge capacity in the second cycle is 183.88 mAh g^{-1}. Usually an irreversible capacity loss would be observed after the first cycle when

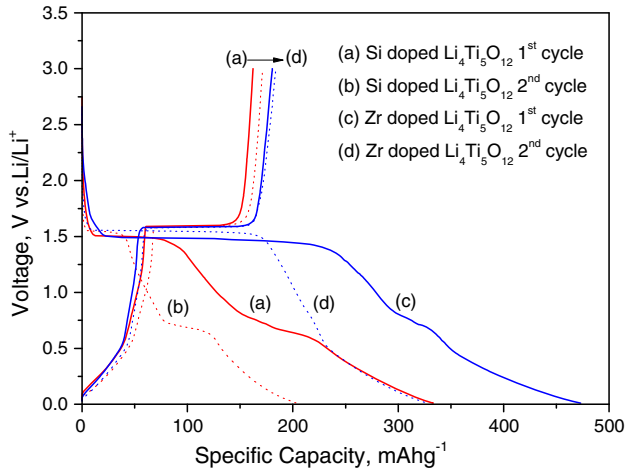

Fig. 7 Charge–discharge curves of Si- (*a* and *b*) and Zr- (*c* and *d*) doped $Li_4Ti_5O_{12}$

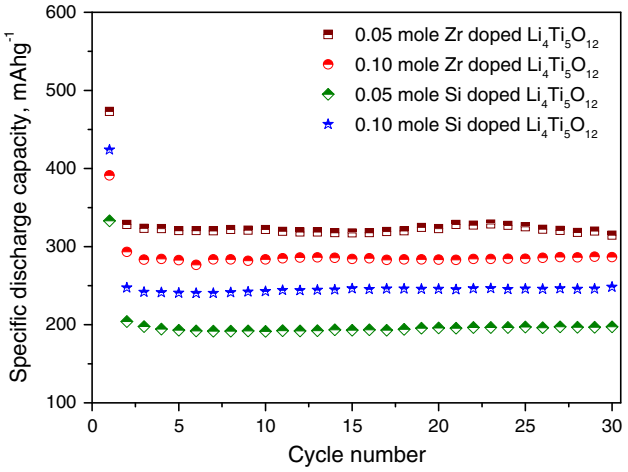

Fig. 8 Cycling stability behavior of undoped and doped $Li_4Ti_5O_{12}$

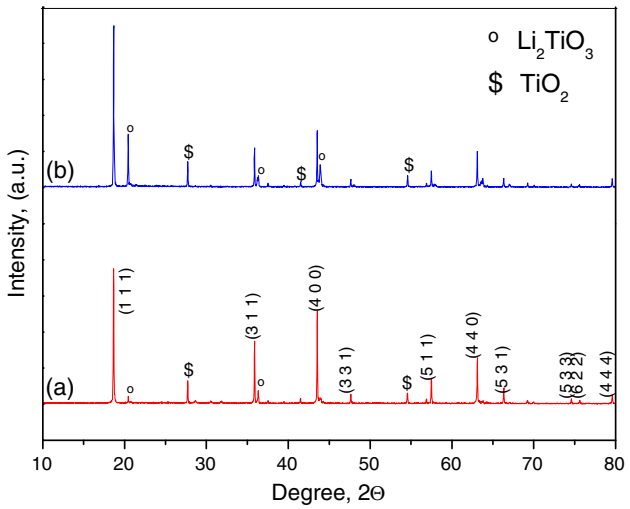

Fig. 9 XRD pattern of Zr (0.10 mol) (**a**) and Si (0.10 mol) (**b**) doped $Li_4Ti_5O_{12}$

discharged to 0 V, mainly due to the SEI layer formed as a reduction of electrolyte to lower potential values. According to the literature, an insertion of additional lithium into the unit cell of $Li_4Ti_5O_{12}$ would cause a lattice expansion by only 0.4 % and the structure is stable enough to provide reversible capacity upon cycling between $Li_4Ti_5O_{12}$ and $Li_{8.5}Ti_5O_{12}$ when discharged to 0 V [44]. There is no possibility for the formation of new phase or the phase separation at this state [45] and the oxidation state of Ti at 0 V is +3 and +4 where the ratio between Ti^{3+} and Ti^{4+} is about 9:1 [46].

As reported earlier [31], the $Li_4Ti_5O_{12}$ exhibits a discharge capacity of 234.5 mAh g^{-1} in the first cycle, corresponding to a coulombic efficiency of 82 %. Herein, the initial discharge capacity values of 333 and 472.9 mAh g^{-1} were observed for Si- and Zr-doped $Li_4Ti_5O_{12}$, which are greater than that of $Li_4Ti_5O_{12}$ (234.6 mAh g^{-1}). The particle size plays an important role in determining the charge capability of the material. When the particle size is reduced, the capacity to accommodate Li ions is increased. As it is observed from FESEM images, there is a uniform distribution of particles along with particle size reduction observed for Zr- and Si-doped $Li_4Ti_5O_{12}$. The uniform distribution of particles in turn enhances the contact between the active material and the electrolyte, which favors the enhanced Li ion and electron transport. The high rate-performance of the material is mainly dependent on these Li ions and electron transport. And this is the reason behind the enhanced electrochemical behavior of Zr- and Si-doped $Li_4Ti_5O_{12}$ compared with pristine $Li_4Ti_5O_{12}$.

The particle size reduction with the Zr^{4+} dopant addition is the main reason for enhancement of the specific capacity of the $Li_4Ti_{4.95}Zr_{0.05}O_{12}$ material. The Zr^{4+} can enter into the lattice site of the pristine and completely stabilize the structure by reducing the change of structure framework during cycling, as observed by Gu et al. [47] for $Li_4Ti_{4.95}Zr_{0.05}O_{12}$/C. The presence of a parasitic Li_2TiSiO_5 phase in the case of Si-modified $Li_4Ti_5O_{12}$ indicates that the Si ions are not completely entered into the lattice site of $Li_4Ti_5O_{12}$. The FESEM image of Si-doped $Li_4Ti_5O_{12}$ shows that there is a segregation of coarse particles due to the presence of Li_2TiSiO_5. However, the particles sizes are reduced to certain extend. From the above results of electrochemical studies, it can be concluded that the appreciable amount of dopant ions are entered into the lattice sites of the host, which are more favorable for enhancing the electrochemical performance of the parent material.

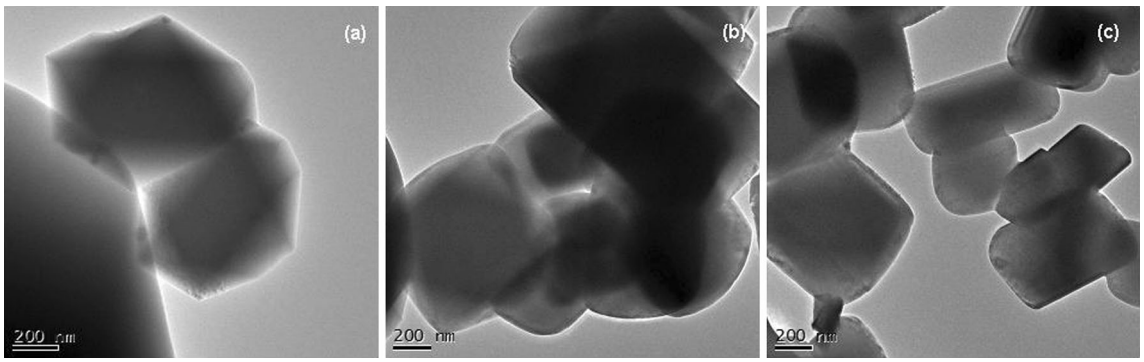

Fig. 10 TEM images of $Li_4Ti_5O_{12}$ (**a**), Zr- (0.10 mol) (**b**), and Si (0.10 mol)- (**c**) doped $Li_4Ti_5O_{12}$

Figure 7 shows the cyclic stability behaviors of Zr- and Si-doped $Li_4Ti_5O_{12}$ in the voltage window between 0 and 3 V for up to 30 cycles. The Zr-doped $Li_4Ti_5O_{12}$ has a high discharge capacity of 472.95 mAh g^{-1} for the first cycle, compared to 333 mAh g^{-1} for Si-doped $Li_4Ti_5O_{12}$ and 234 mAh g^{-1} for $Li_4Ti_5O_{12}$ [31]. The Zr-doped $Li_4Ti_5O_{12}$ showed a high specific capacity and good cyclability compared to those of $Li_4Ti_5O_{12}$ and Si-doped $Li_4Ti_5O_{12}$. The observed capacity of Zr-doped $Li_4Ti_5O_{12}$ is higher than the value reported earlier ($\sim$285 mAh g^{-1}) for $Li_4Ti_{4.95}Zr_{0.05}O_{12}$ prepared with a solution method that is discharged to 0 V by Gu et al. [47]. The main difference arises due to the particle morphology. The observed particles are slightly agglomerated in the solution method. The enhanced performance in our case might be due to the uniform morphology obtained from molten salt synthesis.

In order to further substantiate the results, the electrochemical charge–discharge analysis for higher concentrations of Zr- (0.10 mol) and Si (0.10 mol)-doped $Li_4Ti_5O_{12}$ is carried out and the corresponding cycling stability curve is given in Fig. 8. For Zr (0.1 mol)-doped $Li_4Ti_5O_{12}$, there is a decrease in the specific discharge capacity when compared with 0.05 mol Zr-doped $Li_4Ti_5O_{12}$. The XRD pattern of Zr- and Si (0.10 mol)-doped $Li_4Ti_5O_{12}$ are shown in Fig. 9. The XRD pattern of Zr (0.1 mol)-doped $Li_4Ti_5O_{12}$ elucidates that there is a segregation of additional Li_2TiO_3 and TiO_2 phase compared with Zr (0.05 mol)-doped $Li_4Ti_5O_{12}$ due to the increase in the concentration of Zr^{4+}. Hence it is suggested that, the segregation of these extra phases are unfavorable for enhancing the specific capacity of the material which further concludes the above results that the dopant ions that are not well entered into the lattice sites of the host are unfavorable for enhancing the electrochemical performance of the material.

From the cycling stability curve (Fig. 8) it is also noted that, Si (0.1 mol)-doped $Li_4Ti_5O_{12}$ possess a higher specific capacity values compared with Si (0.05 mol)-doped $Li_4Ti_5O_{12}$ where a higher discharge capacity of 425 mAh g^{-1} with good cycling stability is obtained. The XRD pattern (Fig. 9 (b)) shows that the increase in concentration of Si further enhances the segregation of secondary phase Li_2TiSiO_5. The reason behind the increase in capacity might be arises due to the particle size variation and hence the TEM analysis is carried out for $Li_4Ti_5O_{12}$, Si (0.05 and 0.1 mol)-doped $Li_4Ti_5O_{12}$ and the images are given in Fig. 10. As it is seen from the images, the particles are found to be polyhedron in shape. The TEM image in Fig. 10(b, c) clearly shows that there is a decrease in particle size when the concentration of Si is increased from 0.05 to 0.10 mol. This decrease in particle size is favorable for increase in the specific capacity of the material.

4 Conclusions

Submicron-sized Zr- and Si-doped $Li_4Ti_5O_{12}$ particles were successfully synthesized via a single-step molten salt method. The XRD pattern confirms the formation of cubic spinel structure. Materials with high crystallinity were obtained and found to be micrometers in size without any agglomerations, as observed from the FESEM images. The particle size was reduced upon the addition of dopants Zr^{4+} and Si^{4+}. A maximum value of conductivity was observed for Zr-doped $Li_4Ti_5O_{12}$ (2×10^{-5} S cm^{-1}) compared with Si-doped $Li_4Ti_5O_{12}$ at room temperature. The electrochemical studies based on charge–discharge and electrochemical impedance spectra indicate that Zr- and Si-doped $Li_4Ti_5O_{12}$ possess enhanced Li-ion diffusion and good electrical conductivity compared with those of pristine $Li_4Ti_5O_{12}$. The Zr-doped $Li_4Ti_5O_{12}$ was found to be a superior anode material compared to $Li_4Ti_5O_{12}$ and Si-doped $Li_4Ti_5O_{12}$ because it provided a high discharge capacity and possessed excellent cyclability even with extended cycles.

Acknowledgments This research was supported by a Grant (C12120710) from Gyeonggi Technology Development Program funded by Gyeonggi Province.

References

1. Hanno R, Kawamda (1992) J Electrochem Soc 139:3397
2. Kang YM, Lee SM, Kim SJ, Jeong GJ, Sung MS, Choi WU, Kim SS (2007) Electrochem Commun 9:959
3. Idota Y, Kubota T, Matsufuji A, Maekawa Y, Miyasaka T (1997) Science 276:1395
4. Yoon S, Park C-M, Sohn HJ (2008) Electrochem Solid State Lett 11:A42
5. Wang X, Li X, Sun X, Li F, Liu Q, Wang Q, He D (2011) J Mater Chem 21:3571
6. Courtel FM, Duncan H, Lebdeh YA, Davidson IJ (2011) J Mater Chem 21:10206
7. Chen JS, Archer LA, Lou XWD (2011) J Mater Chem 21:9912
8. Ji S, Zhang J, Wang W, Tang Z (2010) Mater Chem Phys 123:510
9. Bai Y, Wang F, Wu F, Wu C, Bao L (2008) Electrochim Acta 54:322
10. Ying Y, Hao WY, Lai QY, Lu JZ, Chen YD, Ji XY (2008) Ionics 14:85
11. Zhang H, Jin D (2012) Appl Mech Mater 164:293
12. Venkateswarlu M, Chen CH, Lin CW, Choud TC, Hwang BJ (2005) J Power Sources 146:204
13. Cai R, Yu X, Liu XQ, Shao Z (2010) J Power Sources 195:8244
14. Li Y, Zhao H, Tian Z, Qiu W, Li X (2008) J Alloys Compd 455:471
15. Tang Y, Yang L, Fang S, Qiu Z (2009) Electrochim Acta 54:6244
16. Li J, Jin YL, Zhang XG, Yang H (2007) Solid State Ion 178:1590
17. Deng J, Lu Z, Belharouak I, Amine K, Chung CY (2009) J Power Sources 193:816
18. Yi TF, Shu J, Zhu YR, Zhu XD, Ye CB, Zhou AN, Zhu RS (2009) Electrochem Acta 54:7464
19. Zhao H, Li Y, Zhu Z, Lin J, Tian Z, Wang R (2008) Electrochem Acta 53:7079
20. Tian B, Xiang H, Zhang L, Li Z, Wang H (2010) Electrochem Acta 55:5453
21. Qi Y, Huang Y, Ji D, Bao S, Guo ZP (2009) Electrochem Acta 54:4772
22. Shenouda AY, Murali KR (2008) J Power Sources 176:332
23. Huang S, Wen Z, Zhang J, Gu Z, Xu X (2006) Solid State Ion 177:851
24. Hao YJ, Lai QY, Lu JZ, Ji XY (2007) Ionics 13:369
25. Jayaprakash N, Moganty SS, Lou XW, Archer LA (2011) Appl Nanosci 1:7
26. Nugroho A, Chang W, Kim SJ, Chung KY, Kim J (2012) RSC Adv 2:10805
27. Ge H, Li N, Li D, Dai C, Wang D (2009) J Phys Chem C 113:6324
28. Yi TF, Xie Y, Jiang LJ, Shu J, Yue CB, Zhou AN, Ye MF (2012) RSC Adv 2:354
29. Jhan YR, Duh JG (2012) Electrochem Acta 63:9
30. Yi TF, Xie Y, Wu Q, Liu H, Jiang L, Ye M, Zhu R (2012) J Power Sources 214:220
31. Nithya VD, Kalai Selvan R, Kumaran V, Sharmila S, Lee CW (2012) Appl Surf Sci 261:515
32. Scharner S, Weppner W, Beurmann PS (1999) J Electrochem Soc 146:857
33. Akselrud LG, Zavalij PY, Grin Y, Pecharsky VK, Baumgartner B, Wölfel E (1993) Mater. Sci. Forum 133–136:335
34. Deschanvres A, Raveau B, Sekkal Z (1971) Mater Res Bull 6:699
35. Dorrian JF, Newnham RE (1969) Mater Res Bull 4:179
36. Milanovic M, Stijepovic I, Nikolic LM (2010) Process Appl Ceram 4:69
37. Karakassides MA, Gournis D, Petridies D (1999) Clay Miner 34:429
38. Kalai Selvan R, Kalaiselvi N, Augustin CO, Doh CH (2006) Electrochem Solid State Lett 9:A390
39. Jonscher AK (1977) Nature 267:673
40. Li X, Qu M, Yu Z (2009) J Alloys Compd 487:L12
41. Kumar A, Singh BP, Choudhary RNP, Thakur AK (2005) J Alloys Compd 394:292
42. Lee SC, Lee SM, Lee JW, Lee JB, Lee SM, Han SS, Lee HC, Kim HJ (2009) J Phys Chem C 113:18420
43. Tian B, Xiang H, Zhang L, Wang H (2012) J Solid State Electrochem 16:205
44. Zhong Z, Ouyang C, Shi S, Lei M (2008) Chem Phys Chem 9:2104
45. Yao XL, Xie S, Nian HQ, Chen CH (2008) J Alloys Compd 465:375
46. Yi TF, Xie Y, Zhu YR, Zhu RS, Shen H (2013) J Power Sources 222:448
47. Gu F, Chen G, Wang Z (2011) J Solid State Electrochem 16:375